

Individual tree crown segmentation from airborne LiDAR data using a novel Gaussian filter and energy function minimization-based approach

Ting Yun^{a,1}, Kang Jiang^{a,1}, Guangchao Li^a, Markus P. Eichhorn^{b,c}, Jiangchuan Fan^d, Fangzhou Liu^a, Bangqian Chen^e, Feng An^e, Lin Cao^{a,*}

^a Co-Innovation Centre for Sustainable Forestry in Southern China, Nanjing Forestry University, Nanjing 210037, China

^b School of Biological, Earth and Environmental Sciences, University College Cork, Distillery Fields, North Mall, Cork T23 N73K, Ireland

^c Environmental Research Institute, University College Cork, Lee Road, Cork T23 XE10, Ireland

^d National Engineering Research Center for Information Technology in Agriculture, Beijing 100097, China

^e Chinese Academy of Tropical Agricultural Sciences, Ministry of Agriculture, Rubber Research Institute, Danzhou Investigation and Experiment Station of Tropical Crops, Danzhou, China

ARTICLE INFO

Keywords:

Forestry
Individual tree segmentation
Airborne LiDAR
Computer vision
Energy minimization

ABSTRACT

Accurate segmentation of individual tree crowns (ITCs) from airborne light detection and ranging (LiDAR) data remains a challenge for forest inventories. Although many ITC segmentation methods have been developed to derive tree crown information from airborne LiDAR data, these algorithms contain uncertainty in processing false treetops because of foliage clumps and lateral branches, overlapping canopies without clear valley-shape areas, and sub-canopy crowns with neighbouring trees that obscure their shapes from an aerial perspective. Here, we propose an approach to crown segmentation using computer vision theories applied in different forest types. First, a dual Gaussian filter was designed with automated adaptive parameter assignment and a screening strategy for false treetops. This preserved the geometric characteristics of sub-canopy trees while eliminating false treetops. Second, anisotropic water expansion controlled by the energy function was applied for accurate crown segmentation. This utilized gradient information from the digital surface model and explored the morphological structures of tree crown boundaries as analogous to the maximal valley height difference from surrounding treetops. We demonstrate the generality of our approach in the subtropical forests within China. Our approach enhanced the detection rate of treetops and ITC segmentation relative to the marker-controlled watershed method, especially in complicated intersections of multiple crowns. A high performance was demonstrated for three pure *Eucalyptus* plots (a treetop detection rate $r \geq 0.95$ and crown width estimation $R^2 \geq 0.90$ for canopy trees; $r \geq 0.85$ and $R^2 \geq 0.88$ for sub-canopy trees) and three plots dominated by Chinese fir ($r \geq 0.95$ and $R^2 \geq 0.87$ for canopy trees; $r \geq 0.79$ and $R^2 \geq 0.83$ for sub-canopy trees). Finally, in a relatively complex forest park containing a wide range of tree species and sizes, a high performance was also achieved ($r = 0.93$ and $R^2 \geq 0.85$ for canopy trees; $r = 0.70$ and $R^2 \geq 0.80$ for sub-canopy trees). Our method demonstrates that methods inspired by the computer vision theory can improve on existing approaches, providing the potential for accurate crown segmentation even in mixed forests with complex structures.

1. Introduction

Structurally complex forests are a type of woodland in which the arrangement of vegetation is highly varied—the ecosystem includes trees of different sizes, heights, species and ages. Characterizing the forest at the individual tree scale is beneficial for forest resource management, silvicultural system selection and forest yield regulation. Light

detection and ranging (LiDAR) has become a mainstream tool for forest surveys, revealing the three-dimensional structures of trees through a high-resolution representation known as a point cloud. Airborne LiDAR provides a top-down perspective of forests that can be generated over large areas and various terrain conditions (Asner and Mascaro, 2014). Hence, designing an accurate method of detecting and measuring individual tree crowns in complex forests using airborne LiDAR data is a

* Corresponding author.

E-mail address: lincao@njfu.edu.cn (L. Cao).

¹ These authors contributed equally to this work.

prerequisite for scientifically evaluating of forest ecosystems and provides a significant impetus for precision forestry (Holopainen et al., 2014).

The segmentation of individual tree crowns from point clouds generated via Airborne LiDAR is a considerable challenge (Lindberg and Holmgren, 2017). Existing methods can be classified into two categories. The first focuses directly on the scanned points and retrieves the phenotypic and structural characteristics of tree crowns using computer vision techniques. Features such as the point density (Holmgren and Lindberg, 2019), normal vector of the point cloud (Liu et al., 2020) and spatial distribution of the scanned points (Huang et al., 2019), have been employed to fit tree crown models for complex datasets. Principles applied to optimize forest tree segmentation include the extraction of apex properties from tree segments at various spatial scales to exploit crown geometry features (Vega et al., 2014a, 2014b), the calculation of voxel or super voxel features to guild voxel clustering (Ramiya et al., 2019), the analysis of the verticality of the scanned point distribution from the mid and understory layers to identify trunks beneath potential tree crowns (Mongus and Žalik, 2015), and the adoption of the local-projection strategy to detect sub-canopy tree crowns in multi-storied forests (Harikumar et al., 2019).

A second set of approaches maps the scanned points into a planar raster in the form of a digital surface model (DSM) or canopy height model (CHM) and combine image processing or the computer vision technique to realize ITC segmentation. A series of related algorithms has been proposed, such as the marker-controlled-watershed algorithm (Hu et al., 2014), mean-shift clustering algorithm (Dai et al., 2018), graph-cut segmentation algorithm (Strîmbu and Strîmbu, 2015), and the tree crown boundary transformation method based on fishing net dragging (Liu et al., 2015). The concepts behind these algorithms mostly originate from computer vision theory (Jain, 2019) and benefit forest measurements by effectively processing the collected scanned data (Liu et al., 2019).

Despite the numerous approaches proposed to detect treetops and segment individual tree crowns from airborne LiDAR data, each method has both benefits and drawbacks, depending on the specific type of forest. Table 1 provides a brief introduction to the existing methods and highlights three challenges in crown segmentation. (1) Airborne LiDAR provides a top-down scanning perspective and is limited in detecting sub-canopy trees with semi-dwarf tree crowns and hidden features when the line of sight is impeded by vegetative elements in the overstory-layer. (2) Overlapping crowns and mixed-species forests with irregular crown shapes and uncertain margins complicate crown segmentation and reduce the accuracy of crown boundary delineation. (3) More sophisticated tree crown segmentation algorithms demand a greater number of inherent parameters that are either estimated within the method framework or measured directly in the forest field. These parameters also need to be locally calibrated for each forest type and tree species within variable environments and vegetation conditions.

Computer vision is an interdisciplinary scientific field that uses computer theory to gain a high-level understanding of digital images and establish the correlations between 2D images and 3D real-world scenarios (Jain, 2019). Computer vision techniques train machines to extract features from various representations of the studied forest, such as DSM, CHM or point clouds, and provide interpretations of forest scenes from the identified phenotypic and morphological differences between trees to implement individual crown segmentation at varying scales. Energy minimization (Kichenassamy et al., 1995; Liu et al., 2015) is an elegant approach to computer vision problems that have many potential solutions due to uncertainties in the imaging process and ambiguities in visual interpretation. The energy function encodes the problem constraints and seeks its minimum to provide the optimal solution. The concept of energy minimization has been successfully applied in many computer vision applications, such as active contour models for medical image segmentation (Qian et al., 2013), stereo matching from 2D images to 3D scenario reconstruction (Mozerov and

Table 1

Brief introduction to existing methods for crown segmentation from airborne LiDAR data with different point densities, i.e., low (<20 points per m²), medium (20~50 points per m²) and high density (>50 points per m²). DSM: digital surface model; CHM: canopy height model; CF: coniferous forest; BF: broad-leaved forest; MBF: mixed broadleaf-conifer forest.

Category	Typical approaches	Highlights	Drawbacks
Crown segmentation based on the scanned points	(Vega et al., 2014a, 2014b) (Ramiya et al., 2019)	Defining the criteria of apex selection from the scanned points of medium density based on the elevation value and using a distance threshold to guide crown segmentation for CF, BF and MBF. Subdivision strategy for the scanned points of medium density using the super voxel concept and geometrical feature-driven voxel merging and clustering for crown segmentation of MBF.	Relatively poor performance on broad leaved trees due to the higher geometrical complexity of tree crowns with more apices in the crown periphery. Uncertainty exists for the classification algorithm in differentiating canopies of different forest types.
	(Mongus and Žalik, 2015)	Analysing the verticality of the scanned point distribution from high-density point cloud to locate tree trunks, which are taken as the markers, coupled with density-based clustering for crown segmentation for CF, BF and MBF.	The low laser beam penetration rate of caused by occlusion from upper vegetative elements results in weak trunk detection.
	(Harikumar et al., 2019)	A local horizontal projection-based approach designed to optimize the perspective view of the high-density LiDAR data and find sub-canopy tree crowns for CF.	Time-consuming for larger forest areas, and the performance is impaired by low point cloud densities.
Crown segmentation based on the DSM or CHM	(Hu et al., 2014); (Dai et al., 2018)	Marker-controlled watershed method combined with semi-variogram statistics for tree size determination and crown segmentation from the medium-density LiDAR data of MBF. Mean shift segmentation based on the joint feature space of high-density scanned points combined with a semi-supervised classification algorithm for crown segmentation in MBF.	Locally protruding branches cause over segmentation, and lower accuracies occur for deciduous forests with closed canopies. Depending on the number of training samples, failures arise for clustered trees and complex forest architectures.
	(Strîmbu and Strîmbu, 2015)	Retrieval of the topological and hierarchical structure of MBF and construction of a	Parameter settings are important for algorithm performance, and further constraints

(continued on next page)

Table 1 (continued)

Category	Typical approaches	Highlights	Drawbacks
(Liu et al., 2015)	weighted partitioning graph for crown segmentation from medium-density LiDAR data. Refinement of the initial tree crown boundaries of CF and MBF generated by the watershed method from medium-density LiDAR data using the concept of fishing net dragging driven by the height differences between adjacent pixels.	are needed to avoid over- and under-segmentation.	The segmentation accuracy decreases when the gaps between trees do not present marked valley shapes. There is limited detection of small sub-canopy trees.

van de Weijer, 2015) and multi-target detection from multispectral or hyperspectral imageries (Zhu et al., 2020). Tree crown segmentation can be converted into the problem of object segmentation or target detection, and energy minimization has an inherent ability for such applications that can be taken into consideration.

Here, we propose a novel method based on the computer vision theory for accurate tree crown segmentation for a variety of tree species and site conditions, as demonstrated using airborne LiDAR scans of subtropical forests. First, we introduce a new approach to identifying treetops based on a dual Gaussian filter with a screening strategy based on the angle threshold for excluding false treetops detected within the DSM. Second, tree crown segmentation proceeds based on the water expansion concept and an energy control function constituting two items: the gradient information of the DSM and height differences between adjacent treetops and the expansion cells. Finally, our proposed method was applied to different types of forest plot to assess the efficacy of our approach. Through this work, we demonstrate an enhancement of the accuracy of tree crown detection and segmentation relative to existing approaches.

2. Materials and methods

2.1. Study area

Gaofeng Forest is a forest plantation in the Guangxi Province of southern China, covering an area from 108°7' to 108°38' E and 22°49' to 23°5' N. The elevation of the area varies from 78 to 468 m above sea level. The study area covers approximately 52 km². Its topography is composed of mean slope of approximately 29°. There are different types of forest, e.g., pure Eucalyptus (*Eucalyptus robusta* Sm.) forest, Chinese fir (*Cunninghamia lanceolata* Hook.) dominated forests etc. Forests dominated by Chinese fir include some broad-leaved tree species. A Forest park contains a broad mixture of tree species with different crown sizes were also used in this study. They retain small numbers of old trees, e.g., Chinese banyan (*Ficus microcarpa* Blume) and Camphora (*Cinnamomum camphora* (Linn.) J.Presl) with larger and higher tree crowns, and tree saplings (including *Bauhinia*, *Thevetia peruviana* and *Cassia nodosa* etc.), with small plant spacing and some well-pruned small trees of *Loropetalum* spp. planted at the edge of the plot to form a hedge.

According to the historical information provided by the local forest department, saplings of Eucalyptus and Chinese fir were planted on unevenly hilly terrain with equal spacing between the rows or columns. Over the last decades after planting, these trees were affected by variations in environmental conditions, such as irradiance, wind exposure and water flow, and subjected to different management interventions

and reforestation activities, which resulted in a relatively non-uniform growth, variable tree mortality and multi-layered forest structures. Therefore, the two plantation forest types, i.e., pure Eucalyptus and Chinese fir-dominated plots, have small populations (roughly 15–30%) of sub-canopy trees, i.e., trees with narrow or one-sided crowns below the general level of the forest canopy and unable to receive direct light from the sides due to obscuration by surrounding trees. Here, the non-isolated trees that had relatively low heights (<70%) and smaller tree crown widths (<70%) compared with that of the neighbouring trees are considered sub-canopy trees, which are composed of regenerating trees grown in forest gaps with limited growth space and trees with low vigour in terms of competition. Meanwhile, 70–85% of the stems are canopy trees, i.e., trees with full crowns above or equal to the general level of the forest canopy and able to receive direct lights from the sides. For the third type of forest park at the foot of the mountain, there are diverse forest stands and plants at various growth stages under landscape management, constituting a rich vertical structure and beautiful forest sceneries, where approximately 10–20% of the stems are sub-canopy trees.

2.2. Remote sensing data and field data

LiDAR data for the pure Eucalyptus and Chinese fir dominated plots were obtained in January 2018 using a Rigel LMS-Q680i scanner flown at ~750 m above ground level with a strip overlap rate of ~65%. The scanner emits a wavelength of 1550 nm at a 300 kHz pulse repetition rate and a scan frequency of 80 Hz. The beam divergence was approximately 0.5 mrad. Point cloud data for the forest park plot were obtained in February 2018 using a UAV LiDAR. The positional accuracy of this LiDAR dataset was measured by GPS check points. Meanwhile, aerial imageries of the studied forests were also acquired. Fig. 1 shows part of the collected LiDAR data and aerial images of three forest types in our study areas, i.e., pure Eucalyptus forest (Fig. 1 a), Chinese fir-dominated mixed forest (Fig. 1 b) and forest park (Fig. 1 c).

Sampling plots were selected in the study areas, comprising three pure Eucalyptus plots of varying ages and heights grown on the mountain slope with a plot size of 20 × 20 m, three plantations of Chinese fir with a plot size of 20 × 20 m that included other broad-leaf tree species constituted the multi-storied forests. The 7th plot was a subset of a forest park at the foot of a mountain lying on flat terrain and had a size of 136 × 84 m, and it was composed of landscape trees and plants as mentioned in Section 2.1. The field data were collected in January and February 2018.

The positions of the plots were determined using a Trimble R4 GNSS receiver, which was corrected with high-precision real-time differential signals received from the Trimble NetR9 GNSS reference receiver located in an open space near the studied forest plot at a distance of less than 1 km (Shen et al., 2019). A Total station was located at a known point in the plot, and another known point was used for orientation, which facilitated determining the position of tree trunk, resulting in a measurement accuracy of ±10 cm. Tree heights were measured using a Vertex V hypsometer (Haglöf, Långsele, Sweden). Crown widths were obtained by two perpendicular measurements from the location of tree in the east-west and north-south directions. Aerial imageries and point clouds were used as an auxiliary means for the field data. The leaf area index (LAI) of the pure Eucalyptus plots and Chinese fir-dominated plots were indirectly measured using the equipment and cameras with hemispherical lenses (Yun et al., 2016).

2.3. Data processing

An overview of the workflow is shown in Fig. 2. First, the collected airborne LiDAR data for each of the three forest plot types were processed to remove noise and outliers (Xu et al., 2018). A DSM was generated from the scanned points by the rasterization method (Campbell et al., 2020). Next, DSM filtering was performed based on the dual

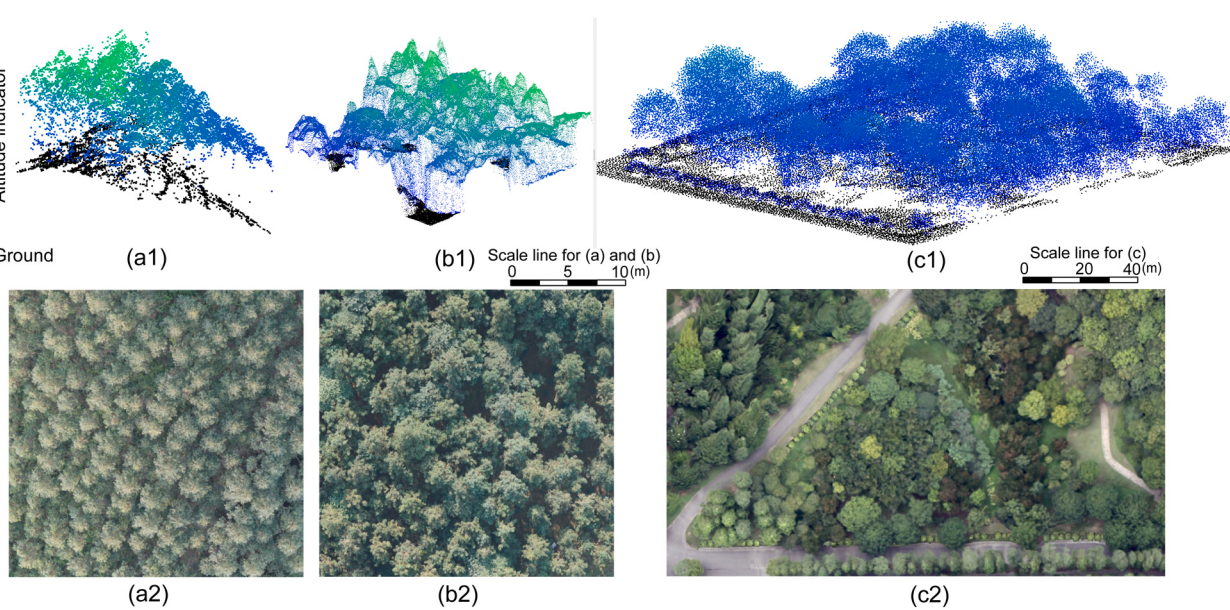


Fig. 1. Airborne LiDAR data and aerial imageries of three forest plot types. (a1) and (a2) Plots of pure Eucalyptus stands of varying sizes and heights. (b1) and (b2) Plots of Chinese fir mixed with other broad-leaved tree species. (c1) and (c2) Subset of a forest park containing larger trees and a shrub layer of sub-canopy stems.

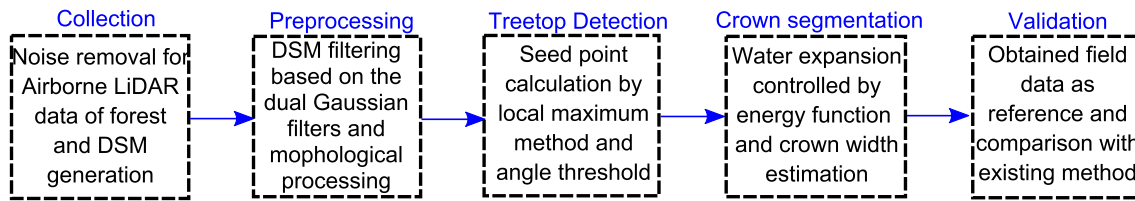


Fig. 2. Flowchart illustrating the main steps of our individual tree crown segmentation method.

Gaussian filter and morphological image processing. Candidate treetops were then detected from the filtered DSM using the local maxima detection method based on the densified point clouds, and a screening strategy based on the angle threshold was employed to exclude false treetops. Then, tree crowns were accurately delineated using a water expansion model controlled by the energy function, and the crown width was estimated in two perpendicular directions. Finally, the performance of our method was compared with that of existing methods and then verified. All steps for the scanned data processing for ITC segmentation were implemented in MATLAB (MathWorks, Inc. Natick, Massachusetts, U.S.A.). The kernel source code was written by the authors and was not derived from any existing package or toolbox in MATLAB; rather, a few existing functions in MATLAB, e.g., “bwboundaries” and “bwperim”, were adopted to display intermediate results and the final extracted boundaries of the tree crowns. The program can be requested from the first and second authors.

2.4. DSM generation

Obtaining an accurate digital terrain model (DTM) from airborne LiDAR in dense forests is difficult due to the poor penetration of laser beams through the forest canopy. Thus, this technology is prone to deviations in the derived CHM. Instead, we used the DSM as the basic data set for our tree crown delineation algorithm. Uniformly distributed and horizontal square grid cells $c \in C$ of size d with the assigned elevation value c_i^z equal to the highest elevation of all scanned tree points within each cell c_i cover the scanned forest plot and make up the corresponding DSM C^z (Khosravipour et al., 2014), where i represents the i th grid cell belonging to the DSM C^z . Usually, the local density of collected forest

point clouds varies with the incident angle of the laser beam, the inclination angles of vegetative elements and the degree of occlusion by obstructing objects (Yun et al., 2019a). The average point density for the forest plots was ~ 120 points per m^2 , therefore a cell (raster) size of 0.18 m was selected to maintain at least 4 points returning for that horizontal extent. This process represented a suitable trade-off between avoiding empty cells and preserving sufficient details to characterise the forest canopy. Consequently, morphological image processing (Bai et al., 2011), which included a dilation operation followed by an erosion operation, was conducted on the DSM to correct the value of the cells with abnormal minimum elevations c_i^z (filling holes) caused by large gaps within a tree crown, which would allow the laser beams to pass through the upper canopy and produce first echo when hitting the understorey vegetation. The morphological processing is also beneficial for suppressing false local maxima generation and maintaining the integrity of the tree crown presence on the DSM (Shamsoddini et al., 2013).

2.5. Tree top detection

Automated methods for identifying tree tops can cause errors in two directions. Large tree crowns with the outermost wild-grown branches attached are often misinterpreted as a group of treetops, which is prone to generating commission errors. On the other hand, groups of small trees can be incorrectly classified as a single tree, creating omission errors. An appropriate filtering solution need to synthetically consider many morphological factors, such as the tree crown size, shape and height; therefore, it is important to enforce both phenotypic and biological properties of the tree crown in the filtering process to facilitate treetop location. We therefore designed a dual Gaussian filter based on

tree height differences and crown shape attributes, which acts to smooth the DSM as follows:

$$D(c) = C(c)^*(G_1(c) + G_2(c)) \quad (1)$$

In Eq. (1), G_1 and G_2 are two Gaussian smoothing filters with an s by s window size based on the distance measure and crown shape variability measure, respectively. These filters are defined as follows: $G_1(c_i) = e^{-d|c_j - c_i|^2/2\sigma_d^2}$ and $G_2(c_i) = e^{-(c_j^z - c_i^z)^2/2\sigma_g^2}$, where c_j belongs to the neighbourhood of c_i , $d|c_j - c_i| \leq s$ is the distance measure between neighbouring cells c_j and c_i , and $(c_j^z - c_i^z)$ uses the height difference measure between the neighbouring cells c_j and c_i to depict the variability in the tree crown shape. The square window size s of two Gaussian smoothing filters can be varied and here s is set as the half of the average crown size of the studied plot, which can be derived from the preliminary forestland survey. The magnitudes of the standard deviations σ_d and σ_g of the two Gaussian smoothing filters are related to the elevation value of the cell c_i on the DSM of the forest plot, i.e., $\sigma_d = a_2 \cdot \sigma_g = a_1 \cdot c_i^z$, where a_1 and a_2 are the weight coefficients.

Fig. 3 demonstrates the basic concept of our filtering process for a variety of tree crowns. Taller trees usually have broader crowns (Fig. 3 a and d). As the standard deviation σ_d of filter G_1 is positively related to the tree height, filter G_1 strengthens the smoothing effect for taller trees and weakens the smoothing effect for smaller or suppressed trees to preserve inconspicuous features of partially blocked crowns (Fig. 3 b). For trees with slender crowns, e.g., *Cedrus deodara* (Roxb.) G. Don and *Metasequoia glyptostroboides* Hu & W.C.Cheng, the smoothing efficiency of filter G_2 will weaken due to an increase in the height differences between adjacent cells of the tree crown, which preserves the phenotypic characteristics and optimizes treetop detection for small trees (Fig. 3 c and d). The combination of the two filters, G_1 and G_2 , is therefore suitable for the DSM of tree crowns with various properties. After smoothing the DSM using our dual Gaussian filter, the locations of candidate treetops at the grid cell level were next identified using a local maxima detection algorithm (Faraji et al., 2015) on the DSM. The detected candidate treetop set may contain some false treetops that present the local maximum heights generated by distinct foliage clumps or strong lateral branches belonging to the same tree crown, as shown in Fig. 3 e. To overcome this problem, a screening strategy for false treetops was proposed. First, a banded neighbourhood, i.e., a long narrow area marked with the orange strip shown in Fig. 3 e and f, along with a line segment connecting each two adjacent candidate treetops with an assigned width (approximately equal to 3 cells) was generated. The grid cell c_i of the local smallest elevation value (the yellow square shown in Fig. 3 e and f) in the corresponding vertical projection area of each

banded neighbourhood on the DSM presents differences in spatial distance and height with the two endpoints c_i' and c_i'' of each line segment (cells containing adjacent candidate treetops labelled by red boxes in Fig. 3 e and f), and then the cell c_i in combination with c_i' and c_i'' forms an included angle $\theta_i(c_i', c_i, c_i'')$ as a quantitative measure. Any single tree typically has a relatively smooth crown shape to increase light exposure and maintain balanced growth to preserve the mechanical stability of the tree body. Hence, when $\theta_i \geq \text{threshold}$, the candidate treetops in the two endpoints c_i' and c_i'' of each line segment were considered to be formed by later branches or separate foliage clumps belonging to the same tree crown, and one candidate treetop should be deleted. Otherwise, the canopy heterogeneity produced by different tree crowns creates gaps between trees, thus leading to a smaller $\theta_i < \text{threshold}$, as shown in Fig. 3 e and f. In addition, if large within-crown gaps among a single sparse tree crown lead to some laser beams penetrating deeply through the upper tree crown and hit some understory or ground vegetation, then certain grid cell in the vertical projection area of the banded neighbourhood may have an extreme local minimal elevation value and the included angle θ may be underestimated. Hence, this method requires prior treatments to suppress these extreme height minimum occurrence inside each tree crown and avoid deviation in the calculated, including morphological image processing for hole filling as mentioned in Subsection 2.4 and the dual Gaussian filtering on the DSM were conducted. After performing this processing, the filtered treetops were taken as seed points for our water expansion algorithm to realize tree crown segmentation.

2.6. Water expansion concept and energy function control

2.6.1. Water expansion concept for segmentation

The pouring water simulation algorithm based on the concept of the marker-controlled watershed method (MCW) from the detected true treetops was used to extract the spatial boundaries of individual tree crowns from the DSM or CHM (Duncanson et al., 2014). This strategy is analogous to the process of pouring water into pits, which are represented by inverse tree crown profiles, and controlling the water flowing into each pit according to the tree heights. The schematic representation in Fig. 4 shows the detailed expansion process from different perspectives. The inverse DSM of each forest plot was vertically and evenly stratified into 5 layers based on an assigned height interval (3.5 m here) and the water was first poured into the lowest layer until it was completely filled. Then the water spreads into the adjacent layer (upper layer) as the water level increases. The process of pouring water continued in this way until the highest layer of each pit was filled with

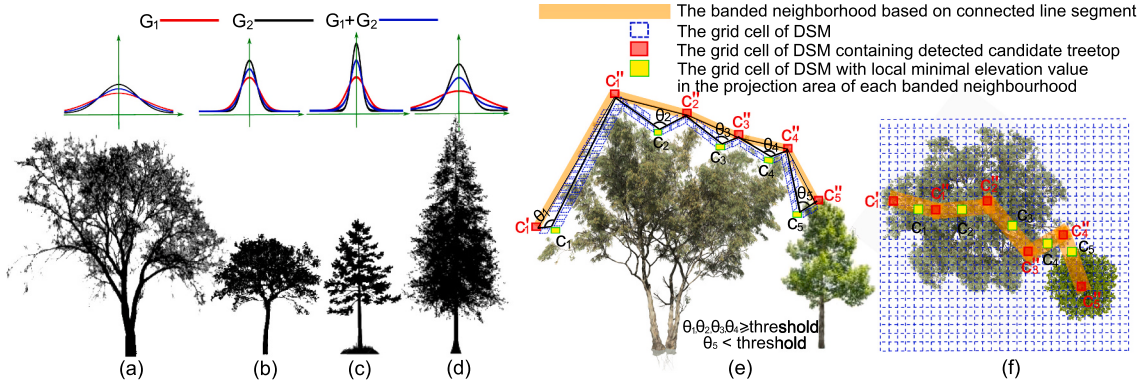


Fig. 3. (a–d) Combination of two Gaussian filters is applied to smooth the airborne LiDAR data of a variety of tree crowns, with filter G_1 based on the distance and G_2 based on the height differences between the adjacent cells of the tree crowns to incorporate variability in crown shapes. (e) and (f) Lateral and top view showing our true treetop selection strategy, respectively. The banded neighbourhood (orange) based on each line segment connecting adjacent candidate treetops with assigned width is designed. The spatial distance and height differences between the grid cell of the local minimal elevation value (yellow grid) in the projection area of each banded neighbourhood and the grid cells containing the corresponding adjacent candidate treetops (red grid) on both sides form the included angle θ , which is taken as a measure to distinguish the true treetops from the candidate treetops.

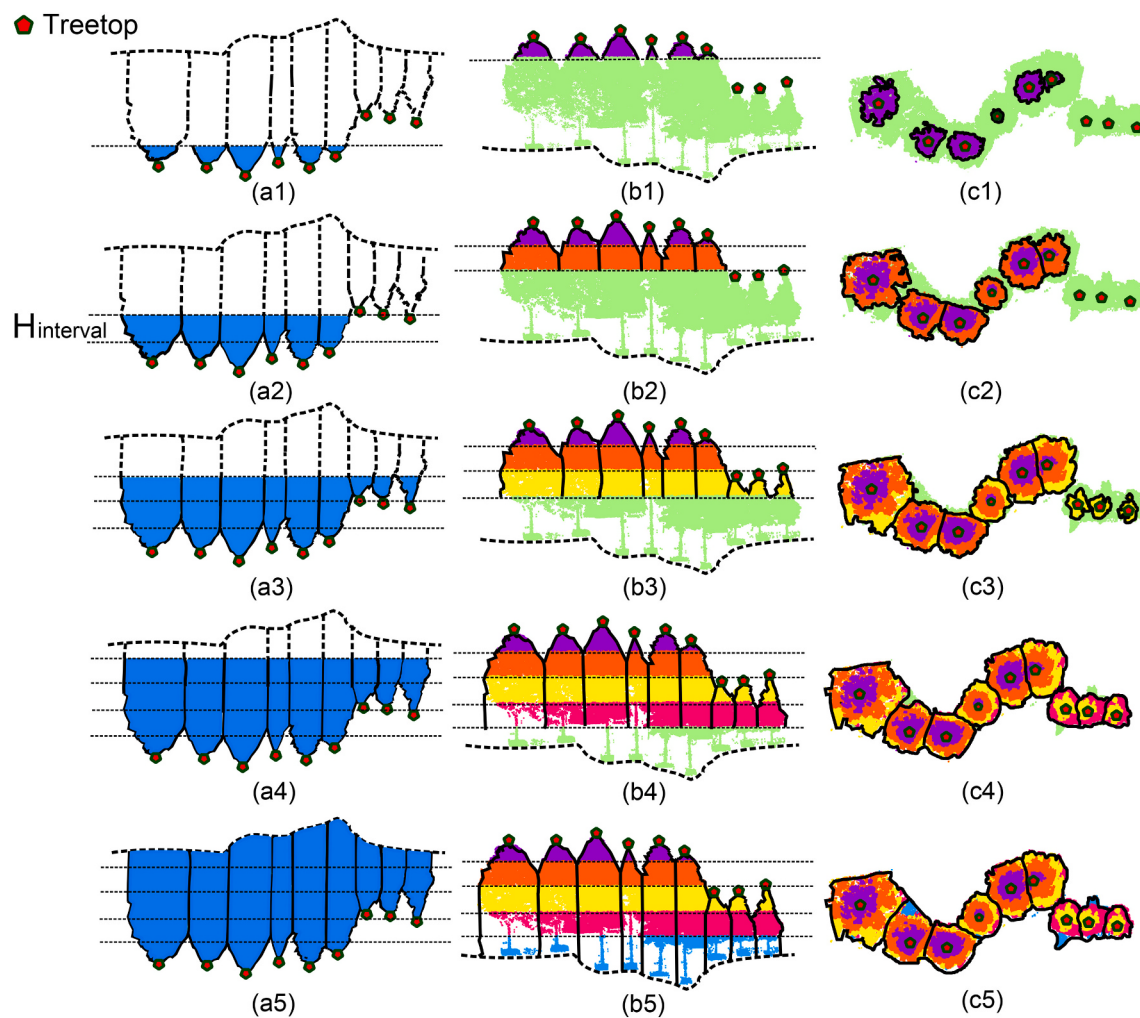


Fig. 4. Schematic representation illustrating the water expansion on the digital surface model for tree crown segmentation. (a) Inverted forest profile represents the concept of water pouring into each tree crown profile. (b) Equivalent figure to (a) but showing that water expansion acts in each height interval in a top-down order. Non-segmented scanned points are represented by the light green colour, and the segmented scanned points are coloured identically. (c) Equivalent figure to (b) but from the top-down view, showing the tree boundary delineation using the watershed method.

water. Tree crown profiles in this region can be clearly delineated through depicting the edge of the water in each pit.

The MCW was originally applied to image segmentation (Yang et al., 2006), which was performed to identify the foreground object and background locations from an image (Parvati et al., 2008). With advancements in interdisciplinary research, the MCW was introduced for processing various types of remote sensing data in the form of 2D arrays, e.g., aerial imagery (Gaetano et al., 2015), DSM (Li et al., 2010) or CHM (Tanhuanpää et al., 2019). The specific implementation of the MCW through programming using MATLAB for realizing tree crown segmentation from LiDAR data can be divided into four steps. First, the MATLAB filter function “imfilter” combined with a single Gaussian-filter is called to smooth the DSM or CHM of the studied forests. Second, the MATLAB function “imregionalmax” is called to identify treetops (local maximum Z value) from the DSM or CHM. Third, the cells within the DSM or CHM are divided into many parts based on the height interval and establishment of the affiliations between each cell and every treetop depending on 8- or 4-neighbourhood cell connectivity. Finally, water expansion is successively fulfilled based on the cell connectivity at every height interval and across the entire DSM or CHM of the forest plots to realize tree crown segmentation.

2.6.2. Energy function for the control of water expansion

Water expansion in each tree crown usually occurs in a random order

at the same height interval. This stochasticity may result in incorrect results, especially when neighbouring trees have intersecting tree crowns within the same height intervals. The absence of clear boundaries and distinct geometric features in the overlapping areas of tree crowns renders precise tree crown segmentation infeasible. Here we propose a method for minimizing such errors.

Tree crown surfaces usually exhibit a downward trend from the treetop to the surrounding areas which continues until the edge of the crown. This suggests three properties that can be used to accurately identify crown boundaries. (1) For any given tree crown cell on the DSM (Fig. 5 a), the gradient vector aligns well with the steepest descent direction from the real treetop to the current cell (Fig. 5 b and c). (2) Tree boundaries can be defined as the valley areas (i.e., elongated depressions or low-lying areas) on the DSM between tree crowns, where maximum height differences with the surrounding treetops occur (Fig. 5 d). (3) Tree crowns form irregular shapes in the horizontal profile. Hence, anisotropic water expansion from the treetop location in each height interval is necessary for accurate tree crown separation.

Based on these three principles, we constructed a Delaunay triangulation of the DSM using the detected true treetops t_k as the triangle vertices. This process vertically subdivides the water expansion for each tree crown into different sections, accounting for its irregular shape (Fig. 5 e). The retrieval of the height differences between the boundary cells of water expansion and the adjacent treetops reasonably transforms

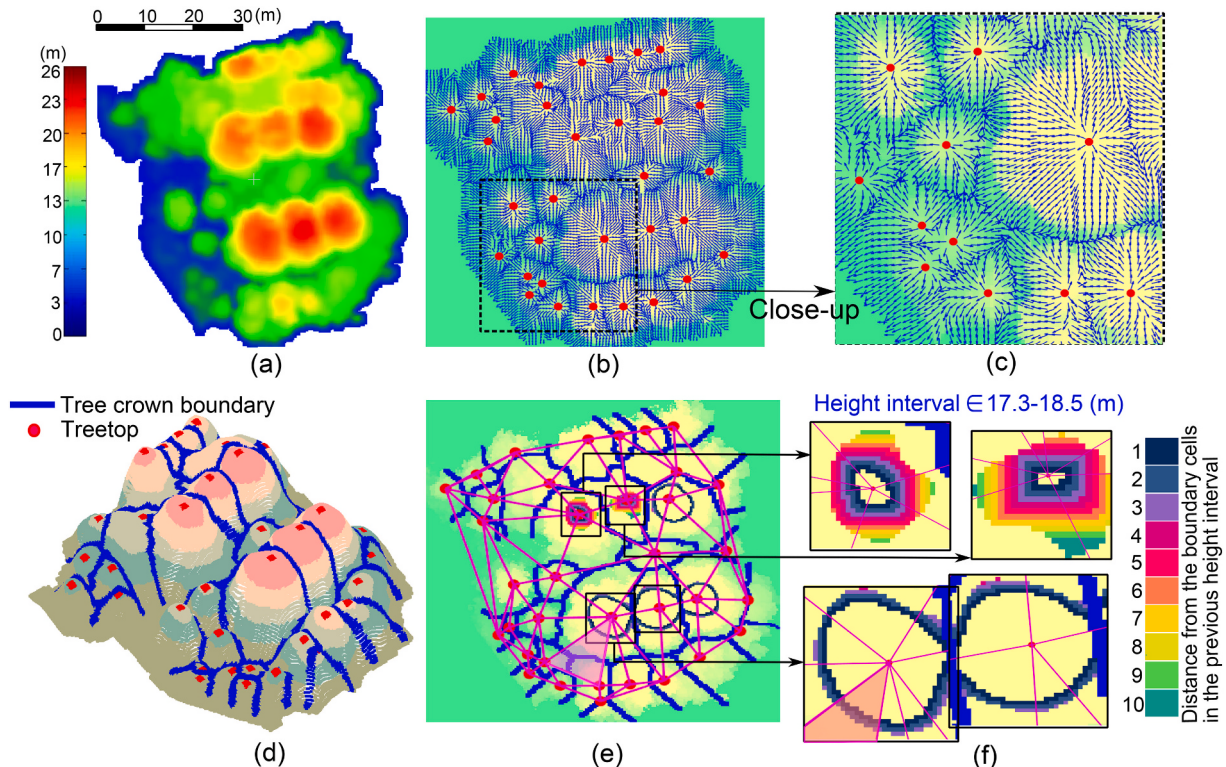


Fig. 5. Schematic diagram illustrating the watershed method controlled by the energy function. (a) DSM generated from airborne LiDAR data after initial filtering. (b) Gradient vector of each DSM cell, which has an approximate direction coincident with the vector from its real treetop to the current cell. (c) Magnification of the black square in (b). (d) True crown boundaries marked in blue, which are located in the valley areas of the DSM and have the maximal heights differences relative to the surrounding treetops. (e) Taking all treetops as the vertices, Delaunay triangulation was performed to refine water expansion control in different triangles, which is beneficial for depicting the anisotropic shapes of tree crowns. (f) Magnification of the four black squares in (e), in which the nested colour contours show synchronous water expansion at the cell scale.

into seeking the height differences between the boundary cells and the three vertices of the triangle in which the boundary cells are located (an example is shown in Fig. 5 e). Thus, an energy function based on the gradient information of the DSM and the height differences was proposed to control the water expansion in each height interval for every tree crown:

$$E_{h_j}(t_k, d) = \frac{1}{n} \sum_{b=1}^n \left\{ \frac{\alpha}{Q_b^k} \cdot \sum_{i=1}^{Q_b^k} \left[\arccos \left(\frac{\overrightarrow{t_k c_{i,d}^b} \cdot \nabla c_{i,d}^b}{|\overrightarrow{t_k c_{i,d}^b}| \cdot |\nabla c_{i,d}^b|} \right) \right] + \frac{\beta}{3} \sum_{l=1}^3 \left(\bar{c}_d^b - t_{c_l^b}^b \right) \right\} \quad (2)$$

where $c_{i,d}^b$ represents the boundary cell of water expansion in the b th triangle of the distance d to the boundary cells of the previous height interval h_{j-1} . Cells c_d , $d = 1, 2, 3\dots$ together form a concentric contour structure through water expansion with the convergent centre of treetop t_k , satisfying the connectivity principle, as shown in Fig. 5f. $c_{i,d}^b$ represents the vertical height of the cell $c_{i,d}^b$. $\nabla c_{i,d}^b$ represents the vector of the maximum gradient of the boundary cell $c_{i,d}^b$ on the DSM C^z and $\overrightarrow{t_k c_{i,d}^b}$ represents the vector from the corresponding treetop location

to the current boundary cell $c_{i,d}^b$. $\arccos \left(\frac{\overrightarrow{t_k c_{i,d}^b} \cdot \nabla c_{i,d}^b}{|\overrightarrow{t_k c_{i,d}^b}| \cdot |\nabla c_{i,d}^b|} \right)$ represents the included angle between the gradient vector of boundary cell $c_{i,d}^b$ and the vector from the starting point of water expansion t_k to the current cell $c_{i,d}^b$. Q_b^k represents the number of current boundary cells $c_{i,d}^b$ in the b th triangle expanded from treetop t_k at distance d . $\sum_{l=1}^3 \left(\bar{c}_d^b - t_{c_l^b}^b \right)$

represents the height differences between the average height value of all water expanded boundary cells $c_{i,d}^b$ and three surrounding treetops $t_{c_l^b}$, i.e., the three vertices of the b th triangle. Here, the coefficient $\alpha \approx 0.1$

and $\beta = \begin{cases} 1 & \text{if } \bar{c}_d^b \searrow \\ -1 & \text{otherwise} \end{cases} : d = 1, 2, 3\dots$, where $\bar{c}_d^b \searrow$ denotes the

monotonic decrease in the average height value of all expanded boundary cells c_d^b in each height interval with increasing distance d .

The gradient vector of each cell as filled through water expansion should be roughly equal to the direction of the vector from the cell to its true treetop, i.e., the included angle between the two vectors should be minimised. Meanwhile, as the water approaches the tree boundary, the height differences between the boundary cells and the three adjacent treetops become larger. Hence, the value of Eq. (2) should maintain a downward trend as distance d increases or the water expansion continues until reaching a minimum value. If an exception occurs and the downward trend is broken, areas generated by incorrect water expansion in the current height interval or distance need to be adjusted such that the order of water expansion for the corresponding tree crowns redistributes correctly among overlapping tree crown areas.

The specific energy function values for each tree crown in the target forest plot illustrated in Fig. 5 are shown in Fig. 6. Fig. 6 a shows that the red contours, i.e., the boundaries of water expansion in each tree crown of every height interval on the DSM, are similar to the structure of the nested hierarchical relationship, i.e., concentric closed contours depicted from the inner to outer tree crown with decreasing height. The blue lines were deliberately drawn to better illustrate the segmented crowns. The energy function values versus the iteration step of the algorithm are shown in Fig. 6 b, where the red lines mark the position of the height interval corresponding to the red contours in Fig. 6 a and the small coloured circle in each height interval in Fig. 6 b represents the detailed

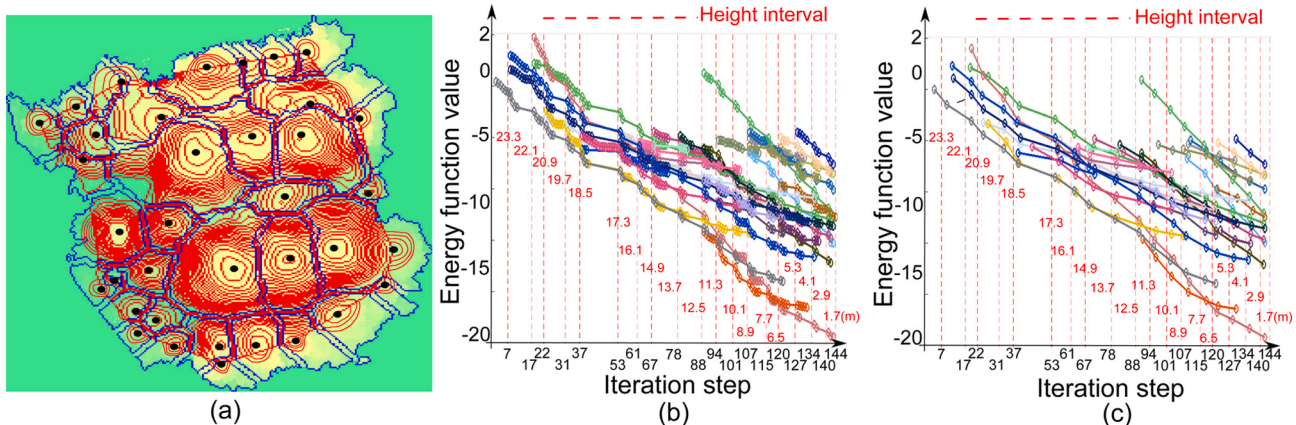


Fig. 6. Process of the water expansion algorithm within each tree crown as controlled by the energy function. (a) Red lines depict the boundaries of water expansion at each height interval, and blue lines represent the final model fit. (b) Values of the energy function for each tree crown with the steps of water expansion. Each coloured line represents a single tree; red vertical dashed lines mark the position of each height interval (as contours in (a)); and coloured circles represent the calculated values of the energy function for the water expanded boundary cells with increasing distance d . (c) Equivalent to (b) but with an abbreviated representation using fewer coloured circles to represent the average value of the energy function in each height interval for every tree crown.

calculated energy function of each concentric contour structure with increased distance d to the boundary of the previous height interval (as the different coloured contours show in Fig. 5 f). Fig. 6 c is a simplified version of Fig. 6 b and uses one small circle to represent the calculated average energy function value of each height interval for every tree crown. The downward trend of the energy function value represents the ability of our method to adaptively control water expansion within each tree crown.

2.7. Assessment of model accuracy

The accuracy of the identification of treetops from airborne LiDAR was assessed against the field measurements using the following equations.

$$r = TP / (TP + FN) \quad (4)$$

$$p = TP / (TP + FP) \quad (5)$$

$$f = 2 \times (r \times p) / (r + p) \quad (6)$$

Here, r (recall) is the tree detection rate, p (precision) is the correctness of the detected trees, f is the overall accuracy of the detected trees, TP (true positive) is the number of correctly detected trees, FN (false negative) is the number of trees that were not detected (omission error), and FP (false positive) is the number of extra trees that did not exist in the field (commission error).

Measures of tree crown widths in the north-south and east-west directions obtained from our method were compared with field data. The accuracy of the estimated tree crown width was assessed by linear regression and evaluated using R-squared, the root mean squared error (RMSE) and the relative root-mean-square error (rRMSE), which is the percentage of the ratio of the RMSE to the observed mean values.

The algorithm performance comparison may be difficult to obtain if various methods are applied on different forest conditions. The MCW mentioned in Section 2.6.1 adopts a single Gaussian filter to smooth the DSM and then combines the local maxima search to detect treetops from the DSM or CHM (Duncanson et al., 2014) (Wan Mohd Jaafar et al., 2018), and it represents a typical algorithm that has been applied in a variety of forest types. Hence, a comparative analysis between the MCW and our approach was conducted on the plots of different forest types.

3. Results

The DSM at a raster resolution of 0.18 m for the sampling plots is

shown in Fig. 7, where 3 equal-sized Eucalyptus plots (Fig. 7 a, b and c) and 3 equal-sized Chinese fir plots (Fig. 7 d, e and f) were arranged in ascending order of stem density with different tree height. Fig. 7 g shows the DSM of the 7th plot of forest park. The specific growth properties of forest stands in the plots are shown in Table 2. An average of 47 (range 24–75) canopy trees and 12 sub-canopy trees (range 5–14) for each plot were present in the six Eucalyptus and Chinese fir plots, with an average density of 0.15 trees/m² (range 0.07–0.22). The forest park was larger in plot size and had more numerous canopy trees (237) and sub-canopy trees (62), with a lower density of 0.03 trees/m² due to the inclusion of some open areas.

3.1. Treetop detection

In Fig. 7, different colours represent the heights relative to the plot ground. Inevitable deviation in the positions between the manually measured trunks and treetops detected by our method occurs because tree trunks can be inclined and GPS errors and LiDAR data positional errors exist. If the horizontal distance between the detected treetops and surrounding trunk locations were larger than half the average tree crown width within the plot, the treetops detected using our method were judged invalid. As seen from Fig. 7, most of the canopy tree and sub-canopy tree treetops were detected by our method.

The rates of treetop detection are shown in Table 2. For the three Eucalyptus plots (a, b and c) and three Chinese fir plots (d, e and f), the treetop detection rates r of canopy trees (0.95–0.97) were similar for Eucalyptus and Chinese fir, and the treetop detection rate r of canopy trees (0.95–0.97) was higher than that of sub-canopy trees (0.79–0.89) because sub-canopy trees are always obscured by taller vegetation and often difficult to differentiate from the surrounding material. Eucalyptus (the first plot type) is a fast-growing hardwood timber species with strong competition for soil nutrient uptake, and these trees form relatively uniformly cylindrical tree crowns with lower mortality rates. These characteristics prevent incursions from other tree species, and a limited forest understory is usually observed. Hence, the simple structures of Eucalyptus trees in plots a, b and c make it easier to detect sub-canopy trees, with $r = 0.85$ –0.89, compared with the structures of the more mixed and structurally complex Chinese fir plots (d, e and f), with $r = 0.79$ –0.80. As a less-profitable silvicultural crop, Chinese fir stands (the second plot type) are commonly neglected or allowed to grow beyond the optimal harvest size. Therefore, mixed-species stands of regenerating broad-leaved trees grow in these plots, with locally protruding branches and multi-foliage clumps, leading to the development of complex, heterogeneous canopies and generating commission errors

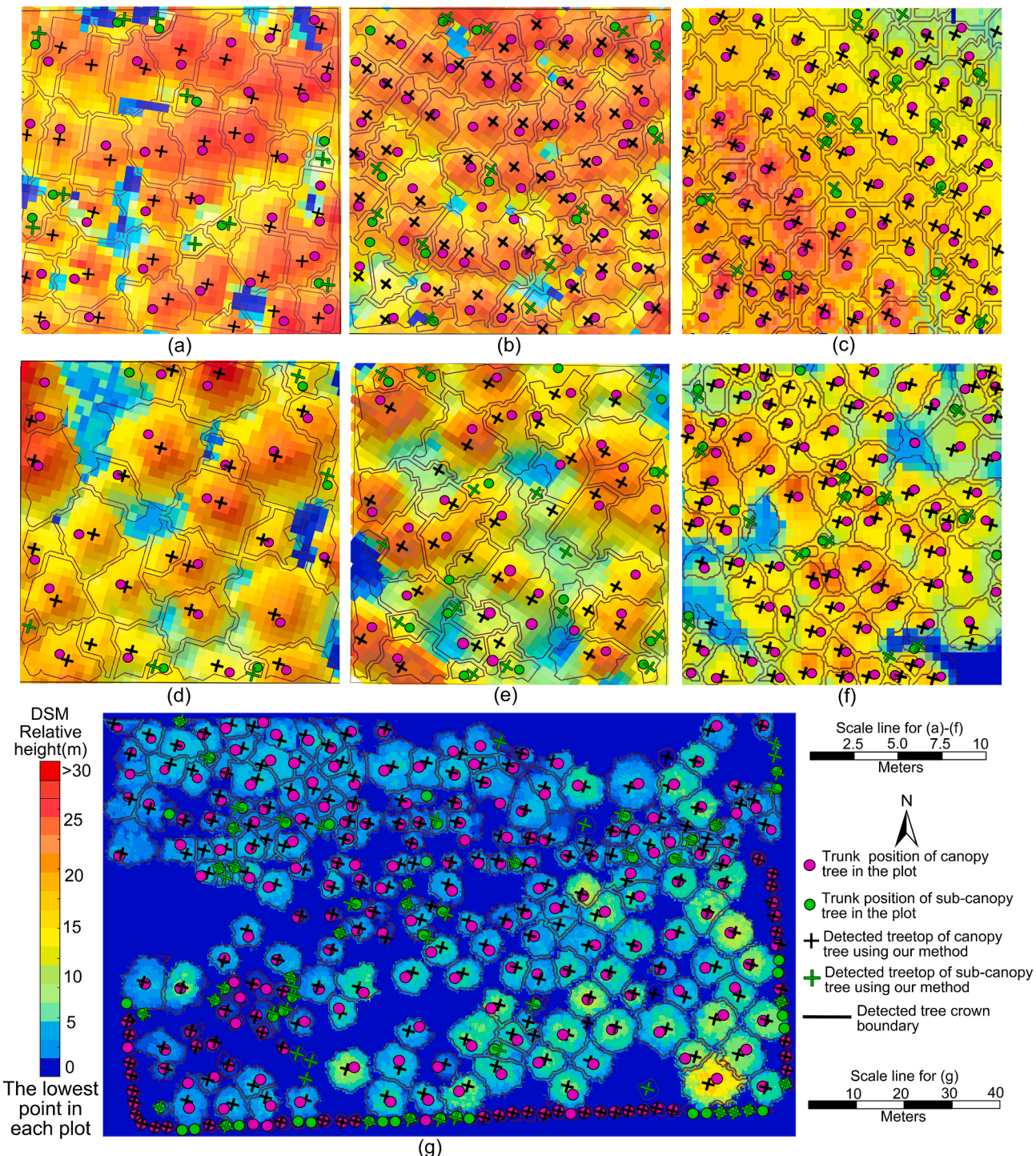


Fig. 7. Treetop detection and crown segmentation for the forest plots. Black lines depict the boundaries of the tree crowns detected using our method. Crosses represent the locations of treetops detected using our method; black: canopy trees; green: sub-canopy trees. Circles represent trunk locations (pink: canopy trees, green: sub-canopy trees). It is reasonable that positional deviation exists between the two kinds of marks for each tree because tree trunks may be skewed or the highest points of trees may be generated by an angled strong branch. (a)-(c) Three pure Eucalyptus plots and (d)-(f) three Chinese fir-dominated plots are arranged by increasing stem densities, respectively. (g) shows a portion of the forest park. (For interpretation of the references to colour in this figure legend, the reader is referred to the web version of this article.)

when detecting treetops. Therefore, the correctness of the detected treetops p for the canopy trees (0.90–0.93) and sub-canopy trees (0.73–0.84) in the three Chinese fir plots was lower than that for the canopy trees (0.91–0.95) and sub-canopy trees (0.80–0.86) in the three Eucalyptus plots, respectively. A small number of omission errors in treetop detection for canopy trees in both Eucalyptus and Chinese fir

plots occurred largely because of natural disturbances, which resulted in damage to canopies and atypical morphological characteristics, or trees located at the edge of the survey plot with one section cut away according to the defined boundaries of the sample plot, which resulted in incompletely scanned tree crowns.

For the 7th plot in the complex forest park (the third plot type),

Table 2

Accuracy assessments for treetop detection in the 7 test forest plots.

Plot	1 a	2 b	3 c	4 d	5 e	6 f	7 g
Density (tree/m ²);	0.11	0.17	0.20	0.07	0.11	0.22	0.03
Proportion of sub-canopy trees	21.4%	19.7%	17.5%	17.2%	31.8%	15.7%	20.7%
Canopy trees							
Number of trees	33	53	66	24	30	75	237
Tree height range (m)	17.2–30.1	14.7–26.7	14.0–22.5	14.5–26.4	11.7–22.8	12.1–19.6	1.3–15.1
NDT	35	54	66	25	32	76	234
TP	32	51	63	23	29	71	221
FP	3	3	3	2	3	5	13
FN	1	2	3	1	1	4	16
r	0.97	0.96	0.95	0.96	0.97	0.95	0.93
p	0.91	0.94	0.95	0.92	0.90	0.93	0.94
f	0.94	0.95	0.95	0.94	0.93	0.94	0.93
Sub-canopy trees							
Number of trees	9	13	14	5	14	14	62
Tree height range (m)	12.6–22.5	13.1–19.7	8.7–14.1	7.6–15.3	8.1–14.7	8.7–12.4	1.3–7.6
NDT	10	13	14	5	15	13	52
TP	8	11	12	4	11	11	43
FP	2	2	2	1	4	2	9
FN	1	2	2	1	3	3	19
r	0.89	0.85	0.86	0.80	0.79	0.79	0.70
p	0.80	0.85	0.86	0.80	0.73	0.84	0.82
f	0.84	0.85	0.86	0.80	0.76	0.81	0.76

Note: NDT: the number of trees detected using our method. TP: the number of correctly detected treetops. FP: the number of extra treetops that did not exist in the field (commission error). FN: the number of treetops that were not detected (omission error). r: the treetop detection rate. p: the correctness of the detected treetops. f: the overall accuracy of the detected treetops.

Table 2 shows a relatively high treetop detection rate *r* of 0.93 and a correctness of the detected treetops *p* of 0.94 for canopy trees, which might be attributed to the regular pruning of mature trees to maintain compact crowns and visually distinguishable tree structures for aesthetic reasons. On the other hand, the treetop detection rate *r* decreased to 0.70 and *p*=0.82 for sub-canopy trees because of the following three factors. First, signs and large stones in the park created point clouds that were falsely identified as tree crowns, generating commission errors. Second, areas of tightly-packed tree saplings in immature canopies presented interlocked crowns, and smaller branches in crowns were misidentified as treetops due to a lack of clear apices in the dense foliage, which easily produce omission and commission errors, respectively. Finally, some small shade-tolerant trees, e.g., *Loropetalum* spp., with heights ≤ 1.5 m and crown widths ≤ 3 m were planted at the edge of the plot beneath larger trees with heights ranging from 8 to 16 m and therefore were occluded from a top-down perspective, thus yielding further omission errors.

3.2. Crown width estimation

Fig. 8 shows the least-squares regression of crown width estimates for the canopy trees and sub-canopy trees obtained by our method against the field measurements. The pure Eucalyptus forest plots had a relatively homogenous structure with leaf area index (LAI) values ranging from 1 to 3. This structure reduces evaporation loss and allows sunlight to reach a larger part of the tree body, and it also enables a relatively clear view of canopy elements from the top-down perspective, thus facilitating the accurate delineation of tree crowns, even beneath the main canopy. Therefore, the three Eucalyptus plots (**Fig. 8 a, b and c**) show a strong correlation and a high degree of correspondence between values. Accurate results were achieved based on the coefficient of determination $R^2 = 0.91 \pm 0.01$, RMSE = 0.26 ± 0.06 m and rRMSE = $9.2 \pm 0.9\%$ for canopy trees and $R^2 = 0.89 \pm 0.02$, RMSE = 0.14 ± 0.04 m and rRMSE = $9.8 \pm 1.5\%$ for sub-canopy trees.

The Chinese fir plots mixed with broad-leaved trees generated greater interspecific competition and more efficient space filling. The vigorous growth of mixed trees causes greater biomass accumulation with higher LAI values ranging from 3 to 5 and yields greater forest dynamics, which results in multiple overlapping crowns and a strong ability for vertical spatial resource capture by the mixed trees, even in areas distant from their stem position. The difficulty of crown

segmentation increases in this environment. In addition, further bias occurs in the field validation of the three Chinese fir plots because manual measurements were obtained in a complex forest with views partially obstructed by dense vegetation elements, and the boundaries of tree crowns are often indistinct due to interlacing branches. It is therefore to be expected that alignment between the two methods would be reduced. Hence, in the three Chinese fir plots (**Fig. 8 d, e and f**), the regression fit of the crown width estimation was slightly weaker for both the canopy trees ($R^2 = 0.89 \pm 0.01$, RMSE = 0.30 ± 0.09 m and rRMSE = $10.9 \pm 1.1\%$) and sub-canopy trees ($R^2 = 0.85 \pm 0.02$, RMSE = 0.13 ± 0.03 m and rRMSE = $12.3 \pm 1.4\%$).

For the forest park, despite the low overall tree density of 0.03 tree/m², the tree distribution was highly clustered and included many open areas for tourists to rest and walk, which reflects that the planting densities differ greatly with the higher species richness in the 7th plot. Variations in plant spreading and plant heights due to artificial arrangement by park growers generates a beautiful landscape and brings occlusion to the forest mid-story component from the top-down views obtained using airborne LiDAR. Hence, many sub-canopy trees (e.g., *Loropetalum* spp.) were mistaken as elements of larger tree crowns, resulting in overestimated crown widths of the canopy trees and underestimated crown widths of the sub-canopy trees. Some canopy trees with multiple trunks were deliberately encouraged to grow in spatially separate foliage clumps, which produce a spurious appearance of multiple tree crowns, thus leading to underestimated crown widths of canopy trees. Hence, a lower level of correlation between the field and airborne LiDAR estimates of crown widths was found in the 7th plot of the forest park for both canopy trees ($R^2 = 0.85 \pm 0.01$, RMSE = 0.63 ± 0.01 m and rRMSE = $13.5 \pm 0.9\%$) and sub-canopy trees ($R^2 = 0.81 \pm 0.01$, RMSE = 0.25 ± 0.01 m and rRMSE = $15.5 \pm 0.03\%$) as shown in **Fig. 8 g**.

At all study sites, a general pattern of underestimating the crown widths was observed for sub-canopy trees. Meanwhile, the crown widths in the east-west and north-south directions obtained using our method were calculated as the lengths of the depicted tree crown domain along two perpendicular axes from the treetop location. When the apex of the treetop is not vertically aligned with the trunk position, which is common for trees exposed to light from the side, we expect to find discrepancies between our approach and in-situ measurements. Such discrepancies can be exaggerated by highly irregular crown drip lines.

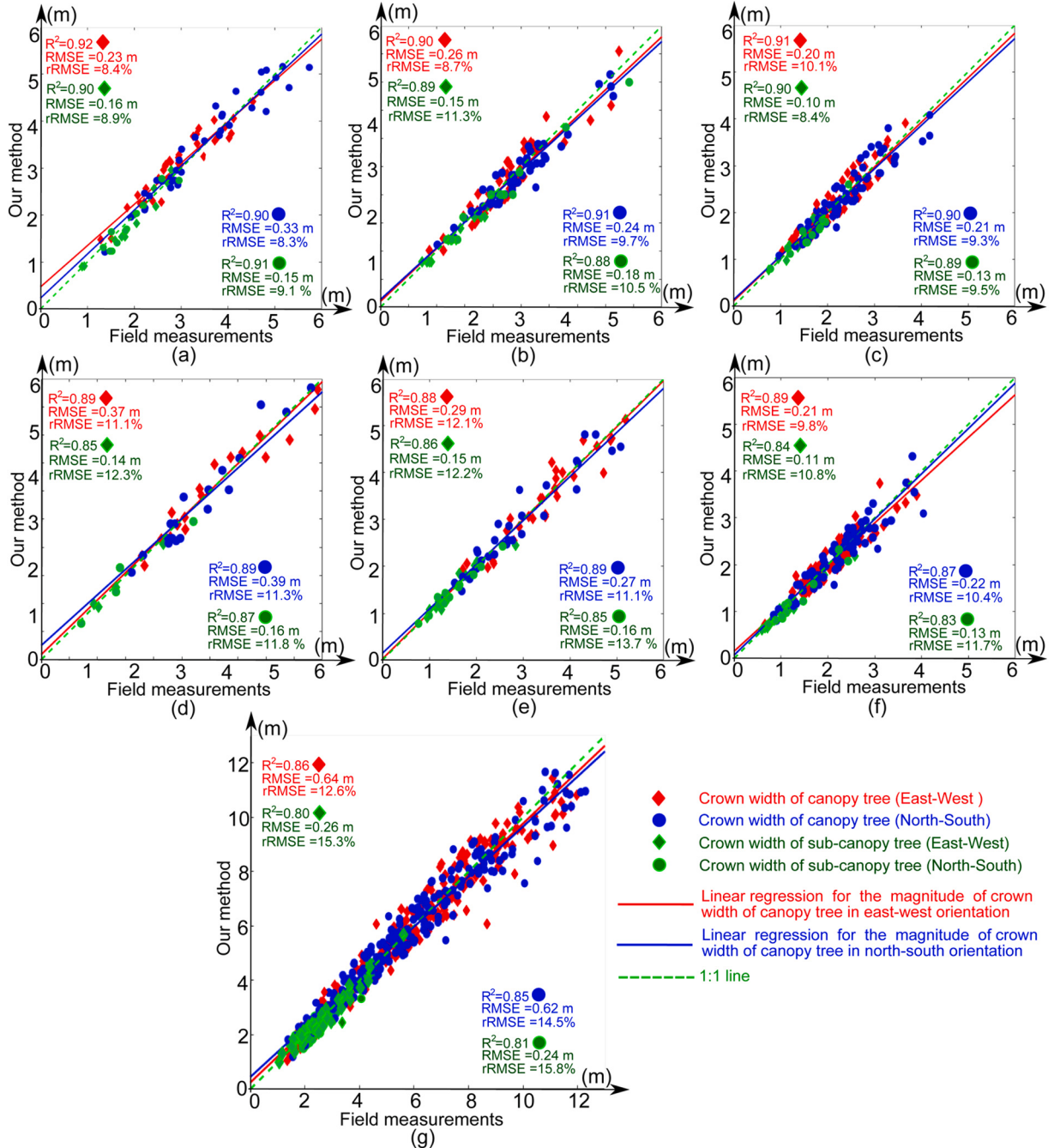


Fig. 8. The scatterplot of the validation of crown width estimation using our method. (a), (b) and (c) Comparison results for Eucalyptus plots 1, 2 and 3 as shown in Fig. 7 a, b and c, respectively. (d), (e) and (f) Equivalent figures for Chinese fir plots 1, 2 and 3 as shown in Fig. 7 d, e and f, respectively. (g) Equivalent figure for the subset of the forest park as shown in Fig. 7 g.

3.3. Comparison with existing methods

We selected one Eucalyptus plot, one Chinese fir plot and the park landscape for a comparative appraisal (plots shown in Fig. 7 c, f and g, respectively) of the crown segmentation performance using our method versus MCW. The results are presented in Fig. 9 and Table 3. In Fig. 9, the light blue borders represent the segmentation results obtained using MCW, and the red borders represent the results obtained using our method.

The magnifications of the tree crown segmentation results for three selected examples in each plot labelled by yellow dashed lines are shown in the middle of Fig. 9, where the segmented trees are highlighted in different colours and pairwise comparisons of the performance of two

methods on the same clustered trees are illustrated. Treetop detection errors are always generated when using the MCW because of the use of a single Gaussian filter on areas with complex canopies, which our method was able to resolve. Fig. 9 a1 shows that the MCW was unable to consistently separate two neighbouring trees marked by deep blue growing on a slope when a continuous height decline created seemingly unbroken crown surfaces while our method was successfully able to separate the two trees with results marked in deep blue and earth-yellow colours. Another source of error in the MCW results was small sub-canopy trees surrounded by larger crowns with features that were hard to distinguish. The omission errors, e.g., the small earth-yellow tree in Fig. 9 a2, the small pink and green trees in Fig. 9 b1 and the small red trees in Fig. 9 b2 identified by our method, were overlooked by the

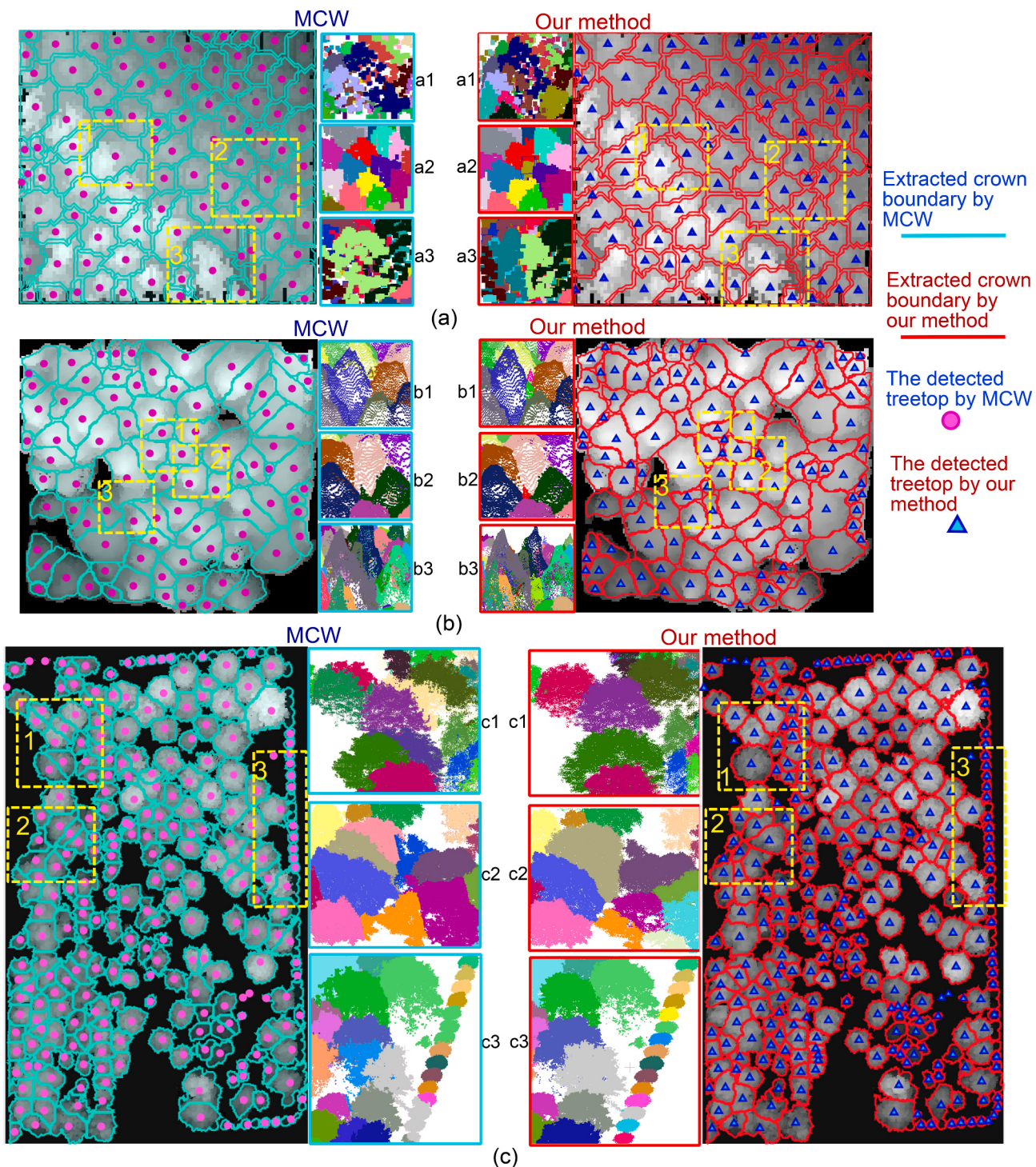


Fig. 9. Airborne LiDAR data from the (a) Eucalyptus plantation, (b) Chinese fir plantation and (c) forest park, corresponding to those in Fig. 7 c, f and g, respectively. Subsections compare the tree crown segmentation results using the marker-controlled watershed (MCW) method labelled by light blue lines versus our method presented in red lines. The magnifications in the middle of each figure illustrate pairwise comparisons of some problematic tree segments, and in all cases, the issues discovered using MCW were overcome or alleviated by our method. These included the prevention of omission errors for small tree crowns with uncertain form and obstructed by adjacent larger crowns (a1, b3 and c3), the detection of sub-canopy trees (a2, b2 and b3), and the separation of complex tree crowns or overlapping foliage (a3, c1 and c2). (For interpretation of the references to colour in this figure legend, the reader is referred to the web version of this article.)

MCW. Finally, the MCW failed to detect when two closely adjacent trees had interlocking crowns, as well as the small trees beneath these crowns (the deep-sky blue tree in a3 and chartreuse small tree in b3 were successfully detected by our method but not by the MCW).

Furthermore, Table 3 demonstrates that some omission errors were overcome after using our dual Gaussian filter for different tree classes.

The treetop detection rate r was 0.95 for canopy trees and 0.86 for sub-canopy trees in the Eucalyptus plot 3c and 0.95 for the canopy trees and 0.79 for the sub-canopy trees in the Chinese fir plot 6f, and these values were markedly higher than those for the canopy trees (0.84 and 0.89) and sub-canopy trees (0.57 and 0.50) in plot 3c and plot 6f achieved using the MCW with a single Gaussian filter process, respectively. The

Table 3

Comparison results of treetop detection and crown delineation using our method versus the marker-controlled watershed method (MCW).

Plot	3 c		6 f		7 g	
Approach	MCW	Our method	MCW	Our method	MCW	Our method
Canopy trees	TP	56	63	68	71	204
	FP	5	3	6	5	27
	FN	10	3	8	4	30
	r	0.84	0.95	0.89	0.95	0.87
	p	0.91	0.95	0.91	0.93	0.88
	R ²	0.855 ± 0.015	0.905 ± 0.005	0.820 ± 0.020	0.880 ± 0.010	0.790 ± 0.030
Sub-canopy trees	TP	8	12	6	11	26
	FP	2	2	2	2	8
	FN	6	2	6	3	36
	r	0.57	0.86	0.50	0.79	0.42
	p	0.80	0.86	0.75	0.84	0.76
	R ²	0.835 ± 0.020	0.895 ± 0.005	0.770 ± 0.015;	0.835 ± 0.005	0.745 ± 0.025

Note: TP: the number of correctly detected treetops. FP: the number of extra treetops that did not exist in the field (commission error). FN: the number of treetops that were not detected (omission error). r: the treetop detection rate. p: the correctness of the detected treetops. R²: the coefficient of determination for tree crown width estimation.

values of *p* in Table 3 also show that the commission error of treetop detection from the existing filtering process was also reduced using our approach due to the additional treetop screening strategy in our filtering process. Meanwhile, errors in treetop detection propagate to the crown width estimation and crown delineation capability of the MCW. Our method was proven superior in processing trees with undulating upper surfaces and shallow gradients. Estimates of the crown width R² for the canopy trees and sub-canopy trees using the MCW were nearly 3–9% lower than those from our approach for the 3c and 6f plots, indicating a greater correspondence of our method with field measurements.

Finally, we considered the landscape of the forest park, where complex canopy structures present challenges for any canopy segmentation algorithm. Fig. 9 c1 shows that the MCW mistakenly separates a single large canopy into several components due to false treetops created by foliage clumps and strong lateral branches, and causes over-segmentation; however, these issues are corrected by our method. Fig. 9 c2 demonstrates that inaccuracies arise through the MCW because asymptotic water expansion only depends on the assigned height interval and connectivity of neighbour cells and an evaluation criterion is not available for the intersection or edge areas. Combined with gradient information, the corresponding result using our method, which is labelled by red boundaries, overcomes the drawbacks and improves the resolution of crown boundary depiction. Fig. 9 c3 exhibits segmentation results in pairs to illustrate the strengthened ability of our method relative to the MCW in sub-canopy tree detection when taller trees extend their canopies over parts of small trees. All these complications resulted in a relatively lower treetop detection rate *r* of 0.42 for sub-canopy trees by the MCW relative to a higher value of 0.70 for *r* using our method. When considering only correctly detected tree crowns, Table 3 shows that our method retains a higher correspondence between estimated and field-measured crown widths compared with the MCW.

4. Discussion

4.1. Segmentation framework and perspective

After conducting experiments on different forest plot types, two major challenges are recognised in identifying tree crowns from airborne laser scanning, and our method addresses these challenges. First, treetop detection errors are common in heterogeneous forest plots, including both omission errors for plots with sub-canopy trees or narrow or sparse crowns, and commission errors for trees with multiple trunks or strong lateral branches. Second, the accuracy of tree crown segmentation declines when neighbouring tree crowns intersect, especially in the overlapping area lacking distinct boundary features. Our method is able to partially compensate for both of these issues, bringing results from airborne LiDAR closer to those obtained from detailed field

surveys.

Many previous studies have addressed the two issues elaborated above. In terms of treetop detection, previous methods have attempted to directly extract 3D point clouds (Vega et al., 2014a, 2014b), and these methods have advantages in recognizing sub-canopy trees when viewed from multiple angles. However, difficulties arise when complications occur, such as when the local conjunction of 3D point clouds impairs the recognition of whole individual crowns (Ramiya et al., 2019), the selection of the direction of the reference plane in the projection is not suitable (Harikumar et al., 2019) and the identification of point clusters that represent single tree crowns or multiple trees is not clear (Amiri et al., 2018). In general, treetop detection methods using 2D CHM or DSM (Yun et al., 2019b) are still convenient and present superior results. However, locating the local maxima with a single-Gaussian filter smoothing may decrease the flexible identification capacity to distinguish sub-canopy trees and minimize the interference derived from locally protruding branches. Therefore, our dual Gaussian filter based on spatial closeness and height differences between the cells combined with a treetop screening strategy enables flexible smoothing for dominant and suppressed trees, which strengthens the smoothing efficacy for larger tree crowns and reserves the traits of the remaining un-occluded portions of small trees as much as possible to facilitate treetop detection; however, additional parameters need to be locally calibrated. Actually, any filtering method (Milanfar, 2013) is likely to present issues when encountering approximately 60,000 potential tree species in numerous types of forests worldwide. Hence, prior knowledge of the study site, such as forest type, tree species, average spacing between trees and average tree crown width, is essential for optimizing the filtering process. Moreover, such knowledge provides guidance for the filter parameter settings, including window size of the smoothing filters, value of the standard deviation and the weights for the two Gaussian filters. Based on the specific situations of the studied forests, the improved filter can lead to better adaptions to the derived DSM or CHM of various forest plots and offer alternative solutions with broader applicability.

In terms of tree crown boundary delineation, ITC segmentation directly from point clouds commonly adopts a clustering algorithm to decompose the airborne LiDAR data into different homogeneous groups (Ferraz et al., 2012). The performance of this kind of algorithm is susceptible to interference from unevenly distributed point clouds, localized data deficiency caused by occlusion and pendulous branches that yield certain conjunctions with neighbouring crowns (Xu et al., 2020a). Meanwhile, methods performed directly on the scanned points that necessarily consider the entire spatial point clouds require more time compared to those based on the CHM or DSM in two dimensions (Aubry-Kientz et al., 2019). On the other hand, some advanced ITC segmentation algorithms based on the CHM or DSM are susceptible to parameter settings, such as multi-weights for the calculation of the edge value of

the connected graph (Strîmbu and Strîmbu, 2015), height-related thresholds and sufficient training samples for various forest types (Liu et al., 2015). These methods bring novel conceptual systems for ITC segmentation but yield new issues behind the theoretical framework that need to be solved (Zhou et al., 2020).

Based on the operational efficiency and general applicability, our method provides a compromise solution for optimizing tree crown segmentation from the perspective of improving the existing MCW approach, although it is affected by the following factors. (1) Different LiDAR point densities present variable levels of crown appearance descriptions and determine the raster cell size of the DSM conveying detailed forest canopy information (Wang et al., 2016). A relatively lower density point cloud paired with a sparse and small tree crown results in some omission errors and blurred edge descriptions. Under a high point density > 100 points per m², Table 3 shows a clear improvement in the detection of the sub-canopy trees (>70%) using our method relative to MCW. (2) Occlusion generally causes less than half of the leaf area to be captured by aerial scanning when the LAI ranges from 3 to 5 (Yun et al., 2019a). These adverse effects impede tree crown width estimation, especially for sub-canopy trees, which results in an underestimation of their crown width (Aubry-Kientz et al., 2019) as shown in Fig. 8, due to the existence of partially blind regions of tree crowns. (3) Taking each treetop as the vertex, the designed strategy of 2D Delaunay triangulation on the DSM was beneficial for separately controlling the water expansion in each tree crown based on various subdivided triangles to better depict the anisotropic shapes of tree crowns (Fig. 5e). Nevertheless, for the trees located at edge areas of the plot without enough adjacent treetops on one side, the resulting obtuse triangle with a narrow area had a certain probability of excessive water expansion that impaired the performance of our method. This method is therefore subject to boundary effects in small plots, although these issues will be reduced with increasing plot size.

Complex forest habitats and terrain conditions always impact the accuracy of DTM retrievals (Gousie and Franklin, 2005). Certain complications, such as increased slope gradient, which adds errors to the LiDAR-derived DTM through an interpolation process (Duan et al., 2015); higher leaf area density, which restricts the visibility of precise terrain information (Xu et al., 2020b); increased tree height, which weakens the LiDAR penetration ability and leads to substantial overestimations of ground elevation (Gatzilolis et al., 2010); dense shrub and herb layers under forest communities, which hide the topographic information of the terrain (Mielcarek et al., 2018), and variations in the specifications of the scanning instruments (all possible return echoes from a waveform signal, energy carried by each pulse, scanning resolution and footprint size) (Gatzilolis et al., 2010), generally produce adverse effects on the estimation of the obtained DEM. Consequently, deviations occur in the derived DTM of dense forests generated from airborne LiDAR data and errors and uncertainties may propagate in the calculated CHM (i.e., the height difference between the ground surface and top of the trees) (Hao et al., 2019). The biased results in the obtained CHM may lead to varying degrees of tree height changes (Okojie et al., 2020) and local deformation of the point cloud geometry within the tree crowns, which results in structural inconsistencies that might affect both the ITC segmentation process and crown attribute characterization (Vega et al., 2014a, 2014b).

Our ITC segmentation method was therefore directly applied to a DSM rather than a CHM. In complex terrains, such as valleys, ridges, escarpments and eroded areas with unclear elevation information regarding where the roots enter the soils, trees can still grow directly upwards and present height-related local maximum traits because trees can detect gravity using tiny structures within the cells of their roots and shoots (Lopez et al., 2014). Therefore, crown segmentation methods (St-Onge et al., 2015; Strîmbu and Strîmbu, 2015) directly applied on the DSM will benefit tree crown detection by maintaining local convexity characteristics and avoid the generation of biased results from the CHM calculation. The only limitation of using the DSM is that the absolute

tree height of a studied forest plot cannot be directly demonstrated from the segmentation results; however, this limitation does not yield unfavourable effects on the final tree crown segmentation results.

4.2. Parameters of our method and algorithm execution

The specific settings for the major parameters in our method are addressed as follows. In the filtering process, our dual Gaussian filter has two adjustable parameters of standard deviations. As tested on 3 different types of forest plots in subtropical forests, the relationship between the two height-related standard deviations σ_d and σ_g can be set as $\sigma_d = a_2 \cdot \sigma_g = a_1 \cdot c_1^2$, where $a_1 \approx 0.3$ and $a_2 \approx 2$. Meanwhile, in the screening process for the false treetop exclusion, the default value of the threshold θ is set to 120°, which is suitable for many tree species in our study plots. If the studied area contains a high proportion of flat-topped tree crowns, e.g., *Albizia julibrissin* Durazz., *Albizia adianthifolia* (Schumach.) W. Wight and *Vachellia sieberiana* (DC.) Kyal. & Boatwr., the value of the threshold θ can be raised by 10° ~ 20°. For the energy control function of Eq. (2), the first item on the right side of the equation affords a complementary criterion based on the gradient information and works on each step of water expansion at the cell level. The value of the first item in radians ranges from 0 to 1.57. In agreement with the variation magnitude of the second item in the height decline at the cell level ranging from 0 to 0.15 m, α is recommended to be a small value of 0.1 ± 0.05 , and $\beta = 1$. For coniferous trees with tower- or column-shaped tree crowns leading to a sharp decline in height with water expansion, a relatively larger value of α is recommended, and vice versa for broad-leaved trees with round or spreading tree crowns.

Our algorithm runs on a computer with the configuration of a Core i7-6700 2.6 GHz Octa-Core Processor, 16 GB RAM, an NVIDIA GeForce GTX 960 graphics card and the Microsoft Windows 8.1 operating system. Taking the 7th plot (Fig. 7 g) as an example, Fig. 10 shows the variations in the RMSE of crown width estimation and time consumption using our method versus the MCW with the changing height interval h_j . The relatively stable trend of the calculated RMSE values using our method for canopy trees and sub-canopy trees is represented by the red solid and dashed lines obtained by cubic polynomial regression fitting shown in Fig. 10, respectively, which illustrate that our method undergoes minor effects from the variation of the tuning parameter h_j due to controlling the water expansion at the cell scale, regardless of the varying value of h_j . In contrast, the pink lines show that the accuracy of crown width estimation using MCW decreases as the parameter h_j increases, which illustrates that a larger height interval in MCW cannot afford fine-scale water expansion control and limits accurate depictions of the edge areas of tree crown. Regarding the aspect of time consumption, the running time of our method is slightly higher than that of the MCW, as shown by the blue lines in Fig. 10. Our approach took

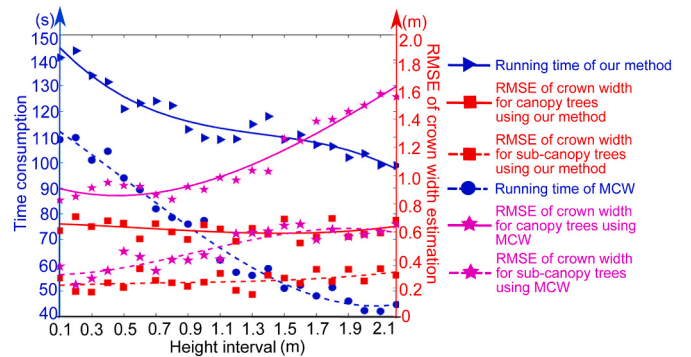


Fig. 10. Dual y-axis plot showing the distribution of the calculated RMSE of the estimated crown width for canopy trees and sub-canopy trees and the programme running time between our approach and the MCW based on the operational height interval. Lines are fitted from cubic polynomial functions.

approximately 40 s longer than the MCW to process the 7th plot (136*84 m), but our method provides more accurate crown width estimates. The time complexity analysis of the MCW and our method and the strategy for conserving time when processing large areas of woodland are discussed in the Supplementary materials.

5. Conclusions

Identifying individual tree crowns in point clouds derived from airborne LiDAR mapping of closed-canopy forests remains a challenge. We have proposed a novel ITC segmentation method based on computer vision theory which combines a dual Gaussian filter and a treetop screening strategy to achieve a flexible filtering process for varying tree sizes and the exclusion of false treetops generated by lateral branches. An energy control function with two constraint conditions, i.e., the height difference and gradient information of the DSM, were built in pursuit of the minimum value of the energy function during the course of water expansion, thus driving the question of crown segmentation toward a better solution. Validation at 7 different forest plots belonging to 3 forest plot types based on the field measurements showed that the treetop detection rate was $\geq 93\%$ for canopy trees and $\geq 70\%$ for sub-canopy trees. Meanwhile, the coefficient of determination R^2 for the tree crown width estimation was ≥ 0.85 for canopy trees and $\geq 0.80\%$ for sub-canopy trees. Our algorithm shows promise for use in detailed mapping over different plot types of closed-canopy broadleaf ecological forests, mixed broadleaf-conifer woodlands and urban forest landscapes that interact with manual intervention. Our method, with its flexibility, and the use of high-performance computer servers, represents a shift toward the possibility of detailed mapping over large areas, and can provide spatial structure information for forest management, carbon stock estimation and habitat mapping.

Funding and acknowledgements

This research was funded by the National Natural Science Foundation of China (grant number 31770591 and 41701510) and the National Key R&D Program of China (grant number 2017YFD0600904). This research was also financially supported by the Central Public-interest Scientific Institution Basal Research Fund for the Chinese Academy of Tropical Agricultural Sciences (grant number 1630022020002). We also would like to thank the graduate students for helping in data collecting and summarising. The authors gratefully acknowledge the local foresters for sharing their rich knowledge and working experience of the local forest ecosystems.

Declaration of Competing Interest

We declare no conflicts of interest with this research.

Appendix A. Supplementary data

Supplementary data to this article can be found online at <https://doi.org/10.1016/j.rse.2021.112307>.

References

- Amiri, N., Polewski, P., Heurich, M., Krzystek, P., Skidmore, A.K., 2018. Adaptive stopping criterion for top-down segmentation of ALS point clouds in temperate coniferous forests. *ISPRS J. Photogramm. Remote Sens.* <https://doi.org/10.1016/j.isprsjprs.2018.05.006>.
- Asner, G.P., Mascaro, J., 2014. Mapping tropical forest carbon: calibrating plot estimates to a simple LiDAR metric. *Remote Sens. Environ.* 140, 614–624. <https://doi.org/10.1016/j.rse.2013.09.023>.
- Aubry-Kientz, M., Dutrieux, R., Ferraz, A., Saatchi, S., Hamraz, H., Williams, J., Coomes, D., Piboule, A., Vincent, G., 2019. A comparative assessment of the performance of individual tree crowns delineation algorithms from ALS data in tropical forests. *Remote Sens.* 11, 1086. <https://doi.org/10.3390/rs11091086>.
- Bai, X., Zhou, F., Xue, B., 2011. Edge preserved image fusion based on multiscale toggle contrast operator. *Image Vis. Comput.* 29, 829–839. <https://doi.org/10.1016/j.imavis.2011.09.003>.
- Campbell, M.J., Dennison, P.E., Tune, J.W., Kannenberg, S.A., Kerr, K.L., Coddington, B.F., Anderegg, W.R.L., 2020. A multi-sensor, multi-scale approach to mapping tree mortality in woodland ecosystems. *Remote Sens. Environ.* 245, 111853. <https://doi.org/10.1016/j.rse.2020.111853>.
- Dai, W., Yang, B., Dong, Z., Shaker, A., 2018. A new method for 3D individual tree extraction using multispectral airborne LiDAR point clouds. *ISPRS J. Photogramm. Remote Sens.* 144, 400–411. <https://doi.org/10.1016/j.isprsjprs.2018.08.010>.
- Duan, Z., Zhao, D., Zeng, Y., Zhao, Y., Wu, B., Zhu, J., 2015. Assessing and correcting topographic effects on forest canopy height retrieval using airborne LiDAR data. *Sensors* 15, 12133–12155. <https://doi.org/10.3390/s150612133>.
- Duncanson, L.I., Cook, B.D., Hurtt, G.C., Dubayah, R.O., 2014. An efficient, multi-layered crown delineation algorithm for mapping individual tree structure across multiple ecosystems. *Remote Sens. Environ.* 154, 378–386. <https://doi.org/10.1016/j.rse.2013.07.044>.
- Faraji, M., Shanbehzadeh, J., Nasrollahi, K., Moeslund, T.B., 2015. Extremal regions detection guided by maxima of gradient magnitude. *IEEE Trans. Image Process.* 24, 5401–5415. <https://doi.org/10.1109/TIP.2015.2477215>.
- Ferraz, A., Bretar, F., Jacquemoud, S., Gonçalves, G., Pereira, L., Tomé, M., Soares, P., 2012. 3-D mapping of a multi-layered Mediterranean forest using ALS data. *Remote Sens. Environ.* 121, 210–223. <https://doi.org/10.1016/j.rse.2012.01.020>.
- Gaetano, R., Masi, G., Poggi, G., Verdoliva, L., Scarpa, G., 2015. Marker-controlled watershed-based segmentation of multiresolution remote sensing images. *IEEE Trans. Geosci. Remote Sens.* <https://doi.org/10.1109/TGRS.2014.2367129>.
- Gatziolis, D., Fried, J.S., Monleon, V.S., 2010. Challenges to estimating tree height via LiDAR in closed-canopy forests: a parable from Western Oregon. *For. Sci.* <https://doi.org/10.1093/forestsce/56.2.139>.
- Gousie, M.B., Franklin, W.R., 2005. Augmenting grid-based contours to improve thin-plate DEM generation. *Photogramm. Eng. Remote. Sens.* 71, 69–79. <https://doi.org/10.14358/PERS.71.1.69>.
- Hao, Y., Zhen, Z., Li, F., Zhao, Y., 2019. A graph-based progressive morphological filtering (GPMF) method for generating canopy height models using ALS data. *Int. J. Appl. Earth Obs. Geoinf.* <https://doi.org/10.1016/j.jag.2019.03.008>.
- Harikumar, A., Bovolo, F., Bruzzone, L., 2019. A local projection-based approach to individual tree detection and 3-D crown delineation in multistoried coniferous forests using high-density airborne LiDAR data. *IEEE Trans. Geosci. Remote Sens.* 57, 1168–1182. <https://doi.org/10.1109/TGRS.2018.2865014>.
- Holmgren, J., Lindberg, E., 2019. Tree crown segmentation based on a tree crown density model derived from airborne laser scanning. *Remote Sens. Lett.* 10, 1143–1152. <https://doi.org/10.1080/2150704X.2019.1658237>.
- Holopainen, M., Vastaranta, M., Hyppä, J., 2014. Outlook for the next Generation's precision forestry in Finland. *Forests* 5, 1682–1694. <https://doi.org/10.3390/f5071682>.
- Hu, B., Li, J., Jing, L., Judah, A., 2014. Improving the efficiency and accuracy of individual tree crown delineation from high-density LiDAR data. *Int. J. Appl. Earth Obs. Geoinf.* 26, 145–155. <https://doi.org/10.1016/j.jag.2013.06.003>.
- Huang, J., Xing, Y., You, H., Qin, L., Tian, J., Ma, J., 2019. Particle swarm optimization-based noise filtering algorithm for photon cloud data in Forest area. *Remote Sens.* 11, 980. <https://doi.org/10.3390/rs11080980>.
- Jain, A.K., 2019. Computer vision. In: *Cutting Edge Technologies and Microcomputer Applications for Developing Countries*. Routledge, pp. 109–117. <https://doi.org/10.4324/9780429042522-10>.
- Khosravipour, A., Skidmore, A.K., Isenburg, M., Wang, T., Hussin, Y.A., 2014. Generating pit-free canopy height models from airborne Lidar. *Photogramm. Eng. Remote. Sens.* 80, 863–872. <https://doi.org/10.14358/PERS.80.9.863>.
- Kichenassamy, S., Kumar, A., Olver, P., Tannenbaum, A., Yezzi, A., 1995. Gradient flows and geometric active contour models. In: *Proceedings of IEEE International Conference on Computer Vision*. IEEE Comput. Soc. Press, pp. 810–815. <https://doi.org/10.1109/ICCV.1995.466855>.
- Li, Y., Zhu, L., Gong, P., Shimamura, H., 2010. A refined marker controlled watershed for building extraction from DSM and imagery. *Int. J. Remote Sens.* <https://doi.org/10.1080/01431160903475373>.
- Lindberg, E., Holmgren, J., 2017. Individual tree crown methods for 3D data from remote sensing. *Curr. For. Rep.* <https://doi.org/10.1007/s40725-017-0051-6>.
- Liu, T., Im, J., Quackenbush, L.J., 2015. A novel transferable individual tree crown delineation model based on fishing net dragging and boundary classification. *ISPRS J. Photogramm. Remote Sens.* 110, 34–47. <https://doi.org/10.1016/j.isprsjprs.2015.10.002>.
- Liu, L., Lim, S., Shen, X., Yebra, M., 2019. A hybrid method for segmenting individual trees from airborne lidar data. *Comput. Electron. Agric.* 163, 104871. <https://doi.org/10.1016/j.compag.2019.104871>.
- Liu, X., Hu, C., Li, P., 2020. Automatic segmentation of overlapped poplar seedling leaves combining mask R-CNN and DBSCAN. *Comput. Electron. Agric.* 178, 105753. <https://doi.org/10.1016/j.compag.2020.105753>.
- Lopez, D., Tocquard, K., Venisse, J.-S., Legué, V., Roeckel-Drevet, P., 2014. Gravity sensing, a largely misunderstood trigger of plant orientated growth. *Front. Plant Sci.* 5 <https://doi.org/10.3389/fpls.2014.00610>.
- Mielcarek, M., Stereńczak, K., Khosravipour, A., 2018. Testing and evaluating different LiDAR-derived canopy height model generation methods for tree height estimation. *Int. J. Appl. Earth Obs. Geoinf.* 71, 132–143. <https://doi.org/10.1016/j.jag.2018.05.002>.
- Milanfar, P., 2013. A tour of modern image filtering: new insights and methods, both practical and theoretical. *IEEE Signal Process. Mag.* 30, 106–128. <https://doi.org/10.1109/MSP.2011.2179329>.

- Mongus, D., Žalik, B., 2015. An efficient approach to 3D single tree-crown delineation in LiDAR data. *ISPRS J. Photogramm. Remote Sens.* 108, 219–233. <https://doi.org/10.1016/j.isprsjprs.2015.08.004>.
- Mozerov, M.G., van de Weijer, J., 2015. Accurate stereo matching by two-step energy minimization. *IEEE Trans. Image Process.* 24, 1153–1163. <https://doi.org/10.1109/TIP.2015.2395820>.
- Okojie, J.A., Okojie, L.O., Effiom, A.E., Odia, B.E., 2020. Relative canopy height modelling precision from UAV and ALS datasets for forest tree height estimation. *Remote Sens. Appl. Soc. Environ.* 17, 100284. <https://doi.org/10.1016/j.rsase.2019.100284>.
- Parvati, K., Prakasa Rao, B.S., Mariya Das, M., 2008. Image segmentation using grayscale morphology and marker-controlled watershed transformation. *Discret. Dyn. Nat. Soc.* 2008, 1–8. <https://doi.org/10.1155/2008/384346>.
- Qian, X., Wang, J., Guo, S., Li, Q., 2013. An active contour model for medical image segmentation with application to brain CT image. *Med. Phys.* 40, 021911 <https://doi.org/10.1118/1.4774359>.
- Ramiya, A.M., Nidamanuri, R.R., Krishnan, R., 2019. Individual tree detection from airborne laser scanning data based on supervoxels and local convexity. *Remote Sens. Appl. Soc. Environ.* 15, 100242. <https://doi.org/10.1016/j.rsase.2019.100242>.
- Shamsoddini, A., Turner, R., Trinder, J.C., 2013. Improving lidar-based forest structure mapping with crown-level pit removal. *J. Spat. Sci.* 58, 29–51. <https://doi.org/10.1080/14498596.2012.759092>.
- Shen, X., Cao, L., Yang, B., Xu, Z., Wang, G., 2019. Estimation of Forest structural attributes using spectral indices and point clouds from UAS-based multispectral and RGB imageries. *Remote Sens.* 11, 800. <https://doi.org/10.3390/rs11070800>.
- St-Onge, B., Audet, F.-A., Bégin, J., 2015. Characterizing the height structure and composition of a boreal forest using an individual tree crown approach applied to photogrammetric point clouds. *Forests* 6, 3899–3922. <https://doi.org/10.3390/f6113899>.
- Strímbu, V.F., Strímbu, B.M., 2015. A graph-based segmentation algorithm for tree crown extraction using airborne LiDAR data. *ISPRS J. Photogramm. Remote Sens.* 104, 30–43. <https://doi.org/10.1016/j.isprsjprs.2015.01.018>.
- Tanhuanpää, T., Yu, X., Luoma, V., Saarinen, N., Raisio, J., Hyppä, J., Kumpula, T., Holopainen, M., 2019. Effect of canopy structure on the performance of tree mapping methods in urban parks. *Urban For. Urban Green.* 44, 126441. <https://doi.org/10.1016/j.ufug.2019.126441>.
- Vega, C., Hamrouni, A., El Mokhtari, A., Morel, M., Bock, J., Renaud, J.-P., Bouvier, M., Durrieu, S., 2014a. PTrees: a point-based approach to forest tree extraction from lidar data. *Int. J. Appl. Earth Obs. Geoinf.* <https://doi.org/10.1016/j.jag.2014.05.001>.
- Vega, C., Hamrouni, A., El Mokhtari, S., Morel, J., Bock, J., Renaud, J.-P., Bouvier, M., Durrieu, S., 2014b. PTrees: a point-based approach to forest tree extraction from lidar data. *Int. J. Appl. Earth Obs. Geoinf.* 33, 98–108. <https://doi.org/10.1016/j.jag.2014.05.001>.
- Wan Mohd Jaafar, W., Woodhouse, I., Silva, C., Omar, H., Abdul Maulud, K., Hudak, A., Klauber, C., Cardil, A., Mohan, M., 2018. Improving individual tree crown delineation and attributes estimation of tropical forests using airborne LiDAR data. *Forests* 9, 759. <https://doi.org/10.3390/f9120759>.
- Wang, Y., Hyypä, J., Liang, X., Kaartinen, H., Yu, X., Lindberg, E., Holmgren, J., Qin, Y., Mallet, C., Ferraz, A., Torabzadeh, H., Morsdorf, F., Zhu, L., Liu, J., Alho, P., 2016. International benchmarking of the individual tree detection methods for modeling 3-D canopy structure for Silviculture and Forest ecology using airborne laser scanning. *IEEE Trans. Geosci. Remote Sens.* 54, 5011–5027. <https://doi.org/10.1109/TGRS.2016.2543225>.
- Xu, Sheng, Xu, Shanshan, Ye, N., Zhu, F., 2018. Automatic extraction of street trees' nonphotosynthetic components from MLS data. *Int. J. Appl. Earth Obs. Geoinf.* 69, 64–77. <https://doi.org/10.1016/j.jag.2018.02.016>.
- Xu, S., Sun, X., Yun, J., Wang, H., 2020a. A new clustering-based framework to the stem estimation and growth fitting of street trees from Mobile laser scanning data. *IEEE J. Sel. Top. Appl. Earth Obs. Remote Sens.* 13, 3240–3250. <https://doi.org/10.1109/JSTARS.2020.3001978>.
- Xu, S., Wang, R., Wang, H., Zheng, H., 2020b. An optimal hierarchical clustering approach to Mobile LiDAR point clouds. *IEEE Trans. Intell. Transp. Syst.* 21, 2765–2776. <https://doi.org/10.1109/TITS.2019.2912455>.
- Yang, X., Li, H., Zhou, X., 2006. Nuclei segmentation using marker-controlled watershed, tracking using mean-shift, and kalman filter in time-lapse microscopy. *IEEE Trans. Circuits Syst. I Regul. Pap.* 53, 2405–2414. <https://doi.org/10.1109/TCSI.2006.884469>.
- Yun, T., An, F., Li, W., Sun, Y., Cao, L., Xue, L., 2016. A novel approach for retrieving tree leaf area from ground-based LiDAR. *Remote Sens.* 8, 942. <https://doi.org/10.3390/rs8110942>.
- Yun, T., Cao, L., An, F., Chen, B., Xue, L., Li, W., Pincebourde, S., Smith, M.J., Eichhorn, M.P., 2019a. Simulation of multi-platform LiDAR for assessing total leaf area in tree crowns. *Agric. For. Meteorol.* 276–277, 107610. <https://doi.org/10.1016/j.agrformet.2019.06.009>.
- Yun, T., Jiang, Kang, Hou, An, Chen, Jiang, Li, Xue, 2019b. Rubber tree crown segmentation and property retrieval using ground-based mobile LiDAR after natural disturbances. *Remote Sens.* 11, 903. <https://doi.org/10.3390/rs11080903>.
- Zhou, Y., Wang, L., Jiang, K., Xue, L., An, F., Chen, B., Yun, T., 2020. Individual tree crown segmentation based on aerial image using superpixel and topological features. *J. Appl. Remote. Sens.* <https://doi.org/10.1117/1.jrs.14.022210>.
- Zhu, L., Wang, L., Ji, L., Yang, W., Geng, X., 2020. Multiple targets inequality constrained energy minimization for multispectral imagery. *Infrared Phys. Technol.* 110, 103465. <https://doi.org/10.1016/j.infrared.2020.103465>.